



HAL
open science

Influence of the fluid–fluid drag on the pressure drop in simulations of two-phase flows through porous flow cells

Maxime Cochenec, Hossein Davarzani, Stéfan Colombano, Ioannis Ignatiadis, Michel Quintard, Yohan Davit

► To cite this version:

Maxime Cochenec, Hossein Davarzani, Stéfan Colombano, Ioannis Ignatiadis, Michel Quintard, et al.. Influence of the fluid–fluid drag on the pressure drop in simulations of two-phase flows through porous flow cells. *International Journal of Multiphase Flow*, 2022, 149, pp.103987. 10.1016/j.ijmultiphaseflow.2022.103987 . hal-03854191

HAL Id: hal-03854191

<https://hal.science/hal-03854191>

Submitted on 15 Nov 2022

HAL is a multi-disciplinary open access archive for the deposit and dissemination of scientific research documents, whether they are published or not. The documents may come from teaching and research institutions in France or abroad, or from public or private research centers.

L'archive ouverte pluridisciplinaire **HAL**, est destinée au dépôt et à la diffusion de documents scientifiques de niveau recherche, publiés ou non, émanant des établissements d'enseignement et de recherche français ou étrangers, des laboratoires publics ou privés.

Numerical simulations of two-phase flows in highly permeable porous media: Effect of permeability on the drag forces at fluid-fluid and fluid-solid interfaces

Maxime Cochenec

Agence de la transition écologique (ADEME), Angers, France

French Geological Survey (BRGM), Orléans, France

*Institut de Mécanique des Fluides de Toulouse (IMFT), Université de Toulouse, CNRS,
France*

Hossein Davarzani, Stéfan Colombano, Ioannis Ignatiadis

French Geological Survey (BRGM), Orléans, France

Yohan Davit*, Michel Quintard

*Institut de Mécanique des Fluides de Toulouse (IMFT), Université de Toulouse, CNRS,
France*

Abstract

To macroscopically describe two-phase flows in porous media we need accurate modeling of the drag forces between the two fluids and the solid phase. In low-permeability porous media, where capillarity is often dominant, the fluid-fluid drag force is treated similarly to the drag between fluids and solid in the momentum transport equation. Two-phase flows in highly permeable porous media, however, are often characterized by a larger interface area between the two fluids and by thin films developing. In such cases, the fluid-fluid drag is not necessarily negligible and may play an important role in

*Corresponding author

Email address: `yohan.davit@imft.fr` (Yohan Davit)

the momentum transport equations. Here, we use computational methods to study immiscible cocurrent two-phase flows in a microfluidic device made of an array of cylinders squeezed between two plates in a Hele-Shaw cell. The key idea is to solve 2D Stokes-Darcy equations integrated over the height of the cell, allowing us to explore different permeability ranges by changing the gap between the plates while keeping the 2D geometry in the cell plane unchanged. We use this approach to ask whether the fluid-fluid drag forces affect the pressure drop and how the flow confinement and the capillary number affect the relative importance of the drag forces. We find different behaviors depending on the gap thickness but, in all cases, the fluid-fluid drag plays a significant role in the pressure drop across the cell.

Keywords: Porous media, Hele-Shaw, Drag forces, Pressure drop

1 **1. Introduction**

2 An accurate description of two-phase flows in high-permeability porous
3 media is of major importance for several practical applications. This in-
4 cludes soil remediation in sandy or gravelly soils (Fetter et al., 2017), nuclear
5 safety (Clavier et al., 2017), and catalytic fixed-bed reactors (de Santos et al.,
6 1991). However, most of the literature on two-phase flows in porous media fo-
7 cuses on low-permeability porous media in the limit of creeping flows, where
8 surface tension forces often dominate and the capillary, Bond, and Weber
9 numbers are low. In that case, the fluid distribution is well described as two
10 independent flow paths for each phase (Dullien, 1992). The two fluids are
11 predominantly segregated with the non-wetting fluid flowing into the large
12 pores and the wetting fluid flowing through the smallest pores. One con-

13 sequence is that the area of the fluid-fluid interface is small (Fig. 1 (a))
14 and that there is little drag between the fluid phases. In contrast, flows in
15 high-permeability porous media are characterized by a complex interaction
16 between capillary, gravity, viscous, and inertial forces (Dullien, 1992; Blunt,
17 2017; Davit and Quintard, 2018). Capillary effects may no longer dominate,
18 and the capillary, Bond, and Weber numbers may be large. The distribution
19 of fluids in the pore space can be schematically decomposed in two modes,
20 even though the reality is often a lot more complex. Either the non-wetting
21 fluid is continuous and flows in the center of the pores surrounded by the
22 wetting fluid flowing as a thin film in contact with the solid (Fig. 1 (b)), or
23 the non-wetting fluid is discontinuous and flows in the center of the pores as
24 droplets or ganglias (Fig. 1 (c)). In both cases, the surface area between the
25 fluids is large and the drag forces between the fluids may be non-negligible
26 compared with the fluid-solid drag forces. This is in strong contrast with
27 capillarity-dominated flow and it is of major importance since modeling of
28 the drag forces is mandatory to build a comprehensive macroscopic model of
29 the flow.

30 *1.1. Generalized Darcy law with coupling*

31 Models used to describe two-phase flows in porous media are often based
32 on a direct extension of Darcy's equations for one-phase flow (Wyckoff and
33 Botset, 1936; Muskat, 1938). This generalization is based upon introducing
34 relative permeabilities, which can be understood as describing the impact
35 of the division of the pore space between the fluids. Each fluid phase acts
36 as a supplementary "solid" regarding the other one and no exchange be-
37 tween the phases is taken into account explicitly (Dullien, 1992; Blunt, 2017).

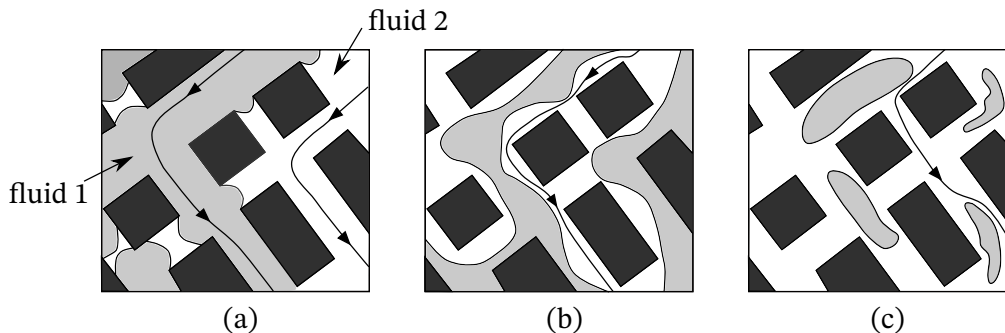


Figure 1: Schematics of example distributions of fluids in a 2D porous network with the solid phase in black, the non-wetting fluid (fluid 1) in light gray, and the wetting fluid (fluid 2) in white, (a) the two fluids are flowing in different channels separated by numerous meniscus and the fluid-fluid interface extent is small, (b) the wetting and non-wetting fluids are flowing together in most of the pores as two continuous streams, and (c) both fluids are flowing together in most of the pores and the non-wetting phase is discontinuous - Figure adapted from Dullien (1992).

38 Consequently, it is commonly assumed that the relative permeability for a
 39 given fluid pair only depends on the saturation (Brooks and Corey, 1964;
 40 Van Genuchten, 1980), even though the relative permeabilities may also de-
 41 pend on the capillary number (Li et al., 2005), the flow regime (Avraam and
 42 Payatakes, 1995; Bianchi Janetti et al., 2017), the viscosity ratio (Yuster
 43 et al., 1951; Ehrlich, 1993; Yiotis et al., 2007) and other properties such as
 44 wettability (Morrow et al., 1973; Anderson et al., 1987; Li et al., 2005). Since
 45 the early 1980s, much work has aimed at improving the generalized Darcy
 46 equations on a sound physical basis. Using upscaling techniques, several
 47 authors have proposed additional coupling terms that correspond to drags
 48 at the fluid-fluid interface and yield coupling permeability tensors (Marle,
 49 1982; Auriault and Sanchez-Palencia, 1986; Whitaker, 1986; Lasseux et al.,

50 1996). The importance of these coupling terms in the overall flow process
51 remains unclear (Ayub and Bentsen, 1999). These additional terms can be
52 calculated analytically in a two-phase annular cocurrent flow in a cylindri-
53 cal capillary tube and are of the same order of magnitude as the dominant
54 relative permeabilities (Bacri et al., 1990). In this theoretical configuration
55 the phase distribution does not depend on the tube radius, i.e., permeability.
56 However, other studies considering more realistic configurations, for which
57 the surface between fluids was smaller, concluded that coupling terms should
58 not be as important (Scott et al., 1953; Rakotomalala et al., 1995; Ayodele,
59 2006). As explained above, this can be linked to the capillarity effect be-
60 ing important, and this effect may be related indirectly to the use of media
61 with sufficiently low permeabilities. Zarcone and Lenormand (1994), Dullien
62 and Dong (1996), and Ramakrishnan and Goode (2015) directly measured
63 the coupling permeability terms in natural media by performing steady-state
64 cocurrent two-phase flows. Rose (1988) proposed indirectly measuring the
65 coupling relative permeability terms by performing two different types of ex-
66 periments. This technique was also used for both cocurrent and counter-
67 current experiments (Bourbiaux et al., 1990; Bentsen and Manai, 1993).
68 These authors (apart from Zarcone and Lenormand) found that the cou-
69 pling relative permeabilities are significant. Using two different experiments
70 raises questions on interpretation, in terms of a unique set of relative perme-
71 abilities and coupling terms, hence the existence of some confusion about the
72 dependence of coupling terms with other physical parameters. In debris-bed
73 cooling studies or flows in trickle-bed reactors, for which the porous media is
74 highly permeable, several projects have shown that including closure terms

75 for the drag force between fluids can better predict measured pressure loss
76 (Schmidt, 2007; Attou et al., 1999). Recently, Clavier et al. (2017) performed
77 experiments of inertial two-phase flows in coarse non-consolidated porous me-
78 dia and proposed constitutive models for the coupling. They were motivated
79 to introduce coupling terms after observing that phases were both flowing
80 within the same pore-space due to the medium’s high permeability. However,
81 in most cases, it is impossible to know from the experiments which type of
82 flow regime dominates at the pore-scale and therefore what is the exact link
83 between the physics at the pore-scale and the macro-scale model.

84 *1.2. Hele Shaw cell*

85 Micromodels can be used to better understand the physics of two-phase
86 flows in porous media (Karadimitriou and Hassanizadeh, 2012), for example,
87 transitions between flow regimes or the onset and development of displace-
88 ment instabilities (Lenormand et al., 1988; Zhang et al., 2011; Horgue et al.,
89 2013). These apparatuses were used to measure the relative coupling perme-
90 abilities for different flow regimes (Avraam and Payatakes, 1995) or study the
91 impact of the fluid-fluid drag on the flow characteristics (Heshmati and Piri,
92 2018; Roman et al., 2019). Rothman (1990) used numerical simulations in a
93 2D micromodel geometry at large capillary numbers and found that coupling
94 permeabilities are comparable in magnitude with the case of the annular flow
95 in a capillary tube. Fig. 2 shows Rothman’s results along with some of the
96 previously mentioned results on relative coupling permeabilities. Given the
97 potential impact of permeability, i.e., characteristic pore length, on phase
98 distribution and hence coupling terms, we also added to the legend of this
99 figure the estimated order of magnitude of the permeability.

100 Hele-Shaw cells are one of the simplest examples of micromodels as they
101 consist of two parallel plates forming a thin gap in which the fluids can flow.
102 Many studies have focused on the displacement of bubbles and droplets in
103 such cells (Maxworthy, 1986; Maruvada and Park, 1996; Kopf-Sill and Homsy,
104 1988) and the stability of the fluid front during the displacement of a fluid
105 by another less viscous fluid (Saffman and Taylor, 1958; Bensimon, 1986;
106 Meiburg and Homsy, 1988; Jackson et al., 2017; Cueto-Felgueroso and Juanes,
107 2014). The governing flow equations are analogous to Darcy’s equation,
108 therefore several studies used Hele-Shaw cells to gain insight about two-phase
109 flow in porous media (Stokes et al., 1986; Homsy, 1987; Liu et al., 2019).

110 *1.3. Outline of the study*

111 In this work, we focus on immiscible cocurrent flow in a modified Hele-
112 Shaw flow cell with obstacles to better capture the physics of porous media
113 flows. We study numerically the influence of the intrinsic permeability on the
114 fluid-fluid and fluids-solid drags for different capillary numbers. To do so, we
115 use a diffuse interface for interface resolving method (Level Set), validated
116 against a Boundary Element Method (BEM) code. The key idea is to vary
117 the thickness of the flow cell to change the permeability without affecting
118 the in-plane geometry. The objective is to quantify the importance of the
119 fluid-fluid drag in two-phase flows in microfluidic devices, and by extension in
120 highly permeable porous media models. In particular, we focus on film-flow
121 regimes; common in highly permeable porous media.

122 The manuscript is organized as follows. The volume-averaged flow equa-
123 tions are derived in Section 2, starting from the 3D flow equations, and then
124 depth-averaged to exhibit a permeability-like term that allows to control the

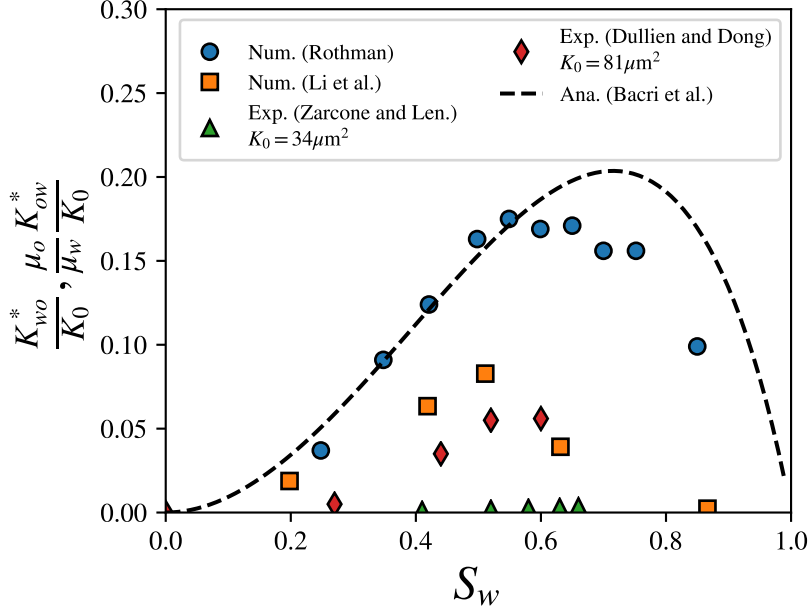


Figure 2: Normalized relative permeabilities for coupling K_{ij}^* as a function of the wetting-fluid saturation S_w from experimental work (Dullien and Dong, 1996; Zarcone and Lenormand, 1994), numerical simulations (Rothman, 1990; Li et al., 2005) and analytical solution for a steady-state annular two-phase flow in a circular capillary tube (dashed line) (Bacri et al., 1990). The theoretical capillary tube case provides an upper limit in terms of permeability and extent of the interfacial surface area between the fluids.

125 fluid-solid drag. In Section 3, the numerical method is introduced as well as
 126 the initial boundary value problem and the mesh convergence study. In Sec-
 127 tion 4, we present the results, the main ones concern the analysis of the drag
 128 forces at the different interfaces as a function of the gap thickness between
 129 the plates.

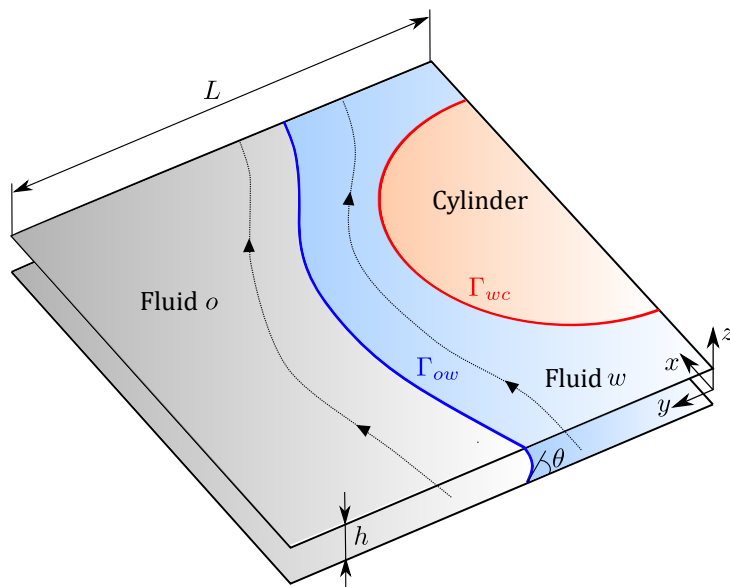


Figure 3: Schematic view of a cocurrent two-phase flow in a Hele-Shaw cell parallel to the $x - y$ plane with a solid obstacle of circular cross-section. L is the transverse dimension of the cell and h is the gap between plates. The boundary between the wetting-fluid w and the cylinder (in red) is noted Γ_{wc} and the boundary between the two fluids (in blue) is noted Γ_{ow} . No dynamic films along the plates are considered here. θ stands for the non-zero contact angle between the two fluids and the plates.

130 2. Pore-scale, depth-averaged and volume-averaged flow equations

131 In this section, we present the derivation of the averaged flow equations
 132 for cocurrent two-phase flows in a Hele-Shaw cell with a solid-phase obstacle
 133 of circular cross-section (Fig. 3). We start from the three-dimensional Stokes
 134 equations. Then, we average the momentum equations spatially to derive the
 135 unclosed form of the macroscopic momentum transport equations.

136 *2.1. Pore-scale flow equations*

137 Three-dimensional continuity and Stokes equations for a Newtonian fluid
 138 in the absence of external forces read, respectively,

$$\nabla^* \cdot \mathbf{u} = 0, \quad -\nabla^* p + \mu \nabla^{*2} \mathbf{u} = 0, \quad (1)$$

139 where the superscript $*$ indicates that the derivative operators are three-
 140 dimensional.

141 *2.2. Depth-averaged flow equations*

142 The starting point is to consider an apparatus such as the one depicted
 143 in Fig. 3, for which h is very small compared to the transverse length of the
 144 cell. It follows that the z -component of the velocity can be neglected (Guyon
 145 et al., 1994), at least sufficiently far away from the obstacle. In consequence,
 146 the three-dimensional velocity is

$$\mathbf{u} = (u(x, y, z), v(x, y, z), 0)^T = (\bar{u}(x, y)f(z), \bar{v}(x, y)f(z), 0)^T, \quad (2)$$

147 where we introduce the depth-averaged, two-dimensional, velocity vector de-
 148 fined as $\bar{\mathbf{u}} \equiv \frac{1}{h} \int_{-h/2}^{h/2} (u(x, y, z), v(x, y, z))^T dz$. The in-plane version of Eq. 1
 149 then reads

$$\nabla \cdot \bar{\mathbf{u}} = 0, \quad -\nabla p + \mu (\nabla^2 \bar{\mathbf{u}} + \bar{\mathbf{u}} f'') = 0. \quad (3)$$

150 where ∇ is now used as a 2D operator. From the condition $\int_{-h/2}^{h/2} f(z) dz = h$,
 151 arising from the definition of the depth-averaged velocity, along with the no-
 152 slip boundary condition at $z \pm h/2$, we find that $f(z) = \frac{3}{2}(1 - 4\frac{z^2}{h^2})$. Then,

$$\nabla \cdot \bar{\mathbf{u}} = 0, \quad \mu (\nabla^2 \bar{\mathbf{u}} - k^2 \bar{\mathbf{u}}) = \nabla p, \quad (4)$$

153 are the continuity and momentum transport equations for the depth-averaged
154 flow of one fluid with $k = \sqrt{12}/h$. Nagel and Gallaire (2015) showed that the
155 velocity profile for a one-phase 3D flow in a rectangular channel is correctly
156 reproduced with the depth-averaged model up to aspect ratios $h/L = 1$. We
157 conducted a similar study in Appendix A, as the solid obstacles are likely
158 to locally disturb the velocity field. We observed a slight deviation between
159 depth-averaged 2D and 3D flows, even for small gaps, which can be attributed
160 to the wall of the cylinders. This discrepancy does not increase with the gap,
161 and the depth-averaged model is effective even for gaps as large as $h/L = 2$.

162 These depth-averaged equations have to be written for each fluid, and
163 boundary conditions at the fluid-fluid interfaces are required to close the
164 problem. Continuity of the depth-averaged velocities across the interface
165 and a jump of the interface normal stress are sufficient conditions if surface
166 tension is constant along the interface. These conditions are expressed as
167 (Park and Homsy, 1984)

$$\bar{\mathbf{u}}_o - \bar{\mathbf{u}}_w = 0 \text{ at } \Gamma_{ow}, \quad (5)$$

$$(\bar{\sigma}_w - \bar{\sigma}_o) \cdot \mathbf{n}_{ow} = \gamma \left(\frac{\pi}{4} \kappa_{\parallel} + \frac{2}{h} \cos \theta \right) \mathbf{n}_{ow} \text{ at } \Gamma_{ow}, \quad (6)$$

168 where $\bar{\sigma}_i = -p_i \mathbf{I} + \mu_i (\nabla \bar{\mathbf{u}}_i + (\nabla \bar{\mathbf{u}}_i)^T)$ is the in-plane stress tensor of fluid i ,
169 \mathbf{n}_{ow} is the in-plane normal vector at the fluid interface pointing toward the
170 fluid w , γ is the surface tension, κ_{\parallel} is the in-plane interface curvature and θ
171 denotes the contact angle between the fluids interface and the plates (Fig. 3).
172 The meniscus in the z -direction is approximated as a half-circle of radius $h/2$
173 and the $\pi/4$ correction for the in-plane curvature was derived by Park and

174 Homsy (1984). In Eq. 6, we neglected the additional terms that pertain to
 175 the formation of the dynamic film and scale non-linearly with the capillary
 176 number. We rather considered a non-zero contact angle, which minimizes
 177 the dynamic film left behind the meniscus.

178 *2.3. Volume-averaged flow equations*

179 Here, we proceed to the spatial averaging of the in-plane momentum
 180 transport equations, following the volume averaging method. This method
 181 has been largely employed for creeping two-phase flows at pore scale, either in
 182 its traditional acceptance (Whitaker, 1986; Lasseux et al., 1996; Chen et al.,
 183 2019) or with additional entropy relation, that is the thermodynamically con-
 184 strained averaging theory (TCAT) (Gray and Miller, 2005, 2014). We recall
 185 that all the flow variables and differential operators have components only
 186 in the transverse direction. According to the volume averaging framework
 187 (Whitaker, 1999) and recalling that Eq. 4 are two-dimensional, the tradi-
 188 tional averaging theorem for the depth-averaged quantity $\bar{\omega}_i$ associated with
 189 the fluid i reads

$$\langle \nabla \bar{\omega}_i \rangle = \nabla \langle \bar{\omega}_i \rangle + \frac{1}{S} \int_{\Gamma_{ic}} \mathbf{n}_{ic} \bar{\omega}_i \, d\Gamma + \frac{1}{S} \int_{\Gamma_{ij}} \mathbf{n}_{ij} \bar{\omega}_i \, d\Gamma, \quad (7)$$

190 where,

$$\langle \bar{\omega}_i \rangle = \frac{1}{S} \int_{S_i} \bar{\omega}_i \, dS, \quad (8)$$

191 is the superficial surface average and S is the surface of a representative ele-
 192 mentary cell. Applying the superficial surface average of Eq. 4 along with the
 193 averaging theorem and using traditional length-scale arguments (Whitaker,
 194 1999) we obtain

$$\nabla \cdot \langle \bar{\mathbf{u}}_i \rangle = 0, \quad i = o, w, \quad (9a)$$

$$\begin{aligned}
& \frac{1}{S} \int_{\Gamma_{ic}} \mathbf{n}_{ic} \cdot \left(-p_i \mathbf{I} + \mu_i \left(\nabla \bar{\mathbf{u}}_i + (\nabla \bar{\mathbf{u}}_i)^T \right) \right) d\Gamma + \\
& \frac{1}{S} \int_{\Gamma_{ij}} \mathbf{n}_{ij} \cdot \left(-p_i \mathbf{I} + \mu_i \left(\nabla \bar{\mathbf{u}}_i + (\nabla \bar{\mathbf{u}}_i)^T \right) \right) d\Gamma - \\
& \mu_i k^2 \langle \bar{\mathbf{u}}_i \rangle = \varepsilon_i \nabla \langle p_i \rangle^i + \langle p_i \rangle^i \nabla \varepsilon_i, \quad i, j = o, w, i \neq j, \quad (9b)
\end{aligned}$$

where \mathbf{I} is the 2×2 identity matrix and $\langle p_i \rangle^i$ ($\langle p_i \rangle^i = \langle p_i \rangle / \varepsilon_i$) is the intrinsic surface average pressure of fluid i , with ε_i the volume fraction of fluid i . The first integral is the drag force exerted upon the obstacle boundary by fluid i and the second integral pertains to the drag force exerted upon fluid j by fluid i . Here, we consider that the contour of the fluid-fluid interface in the $x - y$ plane can be identically translated along the z -direction, which is an approximation since the meniscus is a half-circle for small h/L ratio. If the variation of the saturation in space is negligible and acknowledging that, as illustrated in Fig. 3, only the wetting fluid w is in contact with the obstacle, a more compact form of Eq. 9b reads

$$0 = -\varepsilon_w \nabla \langle p_w \rangle^w - \mu_w k^2 \langle \bar{\mathbf{u}}_w \rangle + \mathbf{d}_{wc} + \mathbf{d}_{wo}, \quad (10a)$$

$$0 = -\varepsilon_o \nabla \langle p_o \rangle^o - \mu_o k^2 \langle \bar{\mathbf{u}}_o \rangle + \mathbf{d}_{ow}, \quad (10b)$$

195 where, \mathbf{d}_{ij} ($\mathbf{d}_{ij} = \frac{1}{S} \int_{\Gamma_{ij}} \boldsymbol{\sigma}_i \cdot \mathbf{n}_{ij} d\Gamma$) denotes the drag forces per unit surface area
196 exerted upon phase j by phase i and which must be computed or modeled
197 to obtain closed macroscopic equations.

198 3. Direct numerical simulations

199 In this section, we introduce the standard Level Set method to capture
200 the moving free interface between the fluids, along with the flow equations,

Drag of... upon...	Fluid o	Fluid w
Plates	$-\mu_o \langle \bar{\mathbf{u}}_o \rangle \frac{12}{h^2}$	$-\mu_w \langle \bar{\mathbf{u}}_w \rangle \frac{12}{h^2}$
Obstacle	-	\mathbf{d}_{wc}
Fluid o	-	\mathbf{d}_{wo}
Fluid w	\mathbf{d}_{ow}	-

Table 1: Summary of drag force terms involved in the averaged momentum transport equation for two-phase flow in a Hele-Shaw cell ($k = \sqrt{12}/h$).

201 both solved with the finite element solver Comsol Multiphysics[®]. In the
 202 following, we are working on the direct calculation of each drag force terms
 203 summarized in Table 1.

204 3.1. Equations

205 The Level Set method is a Eulerian method that easily handles topological
 206 phase changes, in contrast with Lagrangian methods. Here, the fluid phases
 207 are identified with a phase color function that goes smoothly from 0 to 1
 208 across the fluid interface with the manifold defined as the iso-level $\phi = 0.5$.
 209 Transport of the level set function ϕ is governed by

$$\frac{\partial \phi}{\partial t} + \nabla \cdot (\bar{\mathbf{u}}\phi) = \tau \nabla \cdot \left(\psi \nabla \phi - \phi(1 - \phi) \frac{\nabla \phi}{|\nabla \phi|} \right), \quad (11)$$

where $\bar{\mathbf{u}}$ is the depth-averaged velocity field and τ and ψ are two numerical parameters that control the diffuse interface thickness and the amount of initialization of ϕ function, respectively (Olsson and Kreiss, 2005). The same method has been used by Bashir et al. (2014) to reproduced the droplet

generation in a 2D T-junction micromodel. We investigated the accuracy of the implicit definition of the interface and the proper value of the initialization parameter by comparing the interface position to a boundary element method (Nagel and Gallaire, 2015). We found that the inlet velocity is a good value (it is often recommended to start with the maximum magnitude of the velocity expected at the fluid-fluid interface as a first guess). We chose for τ a standard value (Olsson et al., 2007) depending on the maximum size of mesh elements (i.e., $\tau = \max(\Delta x)/2$). The governing flow equations read

$$0 = \nabla \cdot \bar{\mathbf{u}} \quad (12a)$$

$$0 = -\nabla p + \mu(\phi) \left(\nabla^2 \bar{\mathbf{u}} - \frac{12}{h^2} \bar{\mathbf{u}} \right) + \gamma \left(\frac{\pi}{4} \nabla \cdot \left(\frac{\nabla \phi}{|\nabla \phi|} \right) - \frac{2}{h} \right) \delta(\phi) \mathbf{n}, \quad (12b)$$

210 where δ is the Dirac delta function localized on the interface and \mathbf{n} denotes
 211 the unit normal to the interface, respectively defined as,

$$\delta(\phi) = 6 |\nabla \phi| |\phi(1 + \phi)|, \quad \text{and} \quad \mathbf{n} = \frac{\nabla \phi}{|\nabla \phi|}. \quad (13)$$

212 We introduce the following reference and dimensionless quantities,

$$\bar{\mathbf{u}} = \bar{\mathbf{u}}' \times U_r, \quad p = p' \times \frac{\mu_r U_r}{L}, \quad \mathbf{x} = \mathbf{x}' \times L, \quad (14)$$

and the dimensionless continuity and momentum transport equations are

$$0 = \nabla' \cdot \bar{\mathbf{u}}' \quad (15a)$$

$$0 = -\nabla' p' + \frac{\mu(\phi)}{\mu_r} \left(\nabla'^2 \bar{\mathbf{u}}' - \frac{12}{(h/L)^2} \bar{\mathbf{u}}' \right) + \frac{\gamma}{\mu_r U_r} \left(\frac{\pi}{4} \nabla' \cdot \left(\frac{\nabla' \phi}{|\nabla' \phi|} \right) - \frac{2}{h/L} \right) \delta'(\phi) \mathbf{n}, \quad (15b)$$

213 with $\delta'(\phi) = 6 |\nabla' \phi| |\phi(1 + \phi)|$. We therefore have three dimensionless num-
 214 bers: the viscosity ratio $M(\phi) = \frac{\mu(\phi)}{\mu_r}$, the capillary number $Ca^{-1} = \frac{\gamma}{\mu_r U_r}$ and
 215 the aspect ratio $h^* = h/L$.

216 *3.2. Geometry, boundary conditions and simulation parameters*

217 Our macroscopic model is a Hele-Shaw cell with solid obstacles having
 218 cylindrical cross-section. This system is subdivided into seven unit-cell (UC)
 219 subdomains encompassing one obstacle, as depicted in Fig. 4. Seven were
 220 chosen to minimize computational costs based on the observation that, at
 221 steady-state, the impact of inlet and outlet boundaries is nearly limited to
 222 a single unit-cell, and that the phase distribution is quasi-periodic for the
 223 remaining unit cells (see Sec. 4.1). Taking advantage of the symmetry, we
 224 solved only for the upper half of a row. Each fluid flows from left to right (x -
 225 direction) and the inlet boundary conditions for both fluids are a constant
 226 normal inlet velocity u_i . The outlet boundary condition for the flow is a
 227 reference pressure. These boundary conditions are summarized in Table 2.
 228 We choose the sum of the inlet velocity of both fluids as the reference velocity,
 229 so the dimensionless inlet velocities can be expressed as a fractional flow f_f ,

$$f_f = \frac{u_w}{U_t}, \quad u_o = 1 - f_f, \quad \text{with} \quad U_t = u_w + u_o. \quad (16)$$

230 The non-wetting fluid's viscosity was taken as the reference viscosity and the
 231 respective values of the dimensionless parameters are given in Tab. 3. Contact
 232 angle between fluid o (non-wetting) and the solid obstacles is $\theta = 0^\circ$. The
 233 initialization parameter value is equal to the maximum inlet velocity value,
 234 which yields maximum accuracy. As a reference, we conducted numerical
 235 simulations of one-phase flows and found that the gap range used in this
 236 study corresponds to intrinsic permeabilities between 1.5×10^4 and 40 darcy.

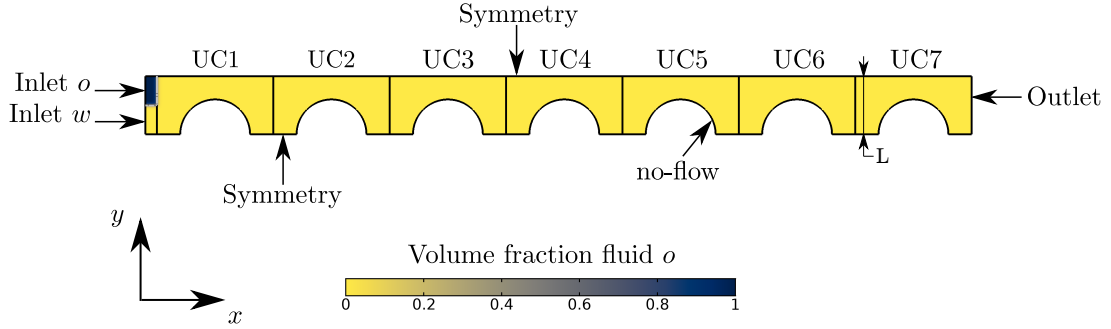


Figure 4: Schematics of geometry and initial conditions. We considered the upper half of an array of seven cylindrical obstacles inside seven cuboids where both fluids are injected from left to right. Initially, the model was saturated with wetting fluid (red), and the width L of one Unit Cell (UC) is 5×10^{-4} m. Symmetry boundary conditions were used on both length sides and the no-flow boundary condition was imposed at the obstacle boundary.

Table 2: Boundary conditions for flow variables and the Level Set function (left) and simulation parameters.

Boundary	u	p	ϕ
Outlet	-	0	$\mathbf{n} \cdot \nabla \phi = 0$
Inlet o	u_o	-	0
Inlet w	u_w	-	1

Table 3: Parameters used for the direct numerical simulations.

Parameters	Value	Physical parameter
$Ca = \frac{U_t \mu_o}{\gamma}$	from 5×10^{-1} to 2.5×10^{-2}	$2.2 \times 10^{-3} \lesssim \gamma \lesssim 4.5 \times 10^{-2}$ mN/m
$M_w = \frac{\mu_w}{\mu_o}$	1	$\mu_o = 10^{-3}$ Pa.s
$f_f = \frac{u_w}{U_t}$	1/4	$U_t = 8 \times 10^{-4}$ m/s
$h^* = h/L$	from 5 to 1/20 and 2D case	$L = 5 \times 10^{-4}$ m

237 3.3. Mesh sensitivity analysis

238 Here, we study the mesh convergence of drag forces and averaged velocity.
239 Three cases were investigated : (*case A*) $Ca = 1.25 \times 10^{-1}$, $h^* = 1/4$, (*case*
240 *B*) $Ca = 2.5 \times 10^{-2}$, $h^* = 1/10$ and (*case C*) $Ca = 5 \times 10^{-1}$, $h^* = 5$. Other
241 parameters are kept constant, i.e., $f_f = 0.25$ and $M = 1$. In Fig. 5 the results
242 are normalized with respect to those obtained from the finest mesh and are
243 given as a function of the relative number of mesh elements in the whole
244 model, starting from 1000 triangular mesh elements as a basis. The fluid-
245 fluid interface position for three different meshes is given in Fig. 5 (d) for
246 the fourth unit-cell (UC4) and *case B*. We found that the drag terms are not
247 very sensitive to the mesh density and that the interface between the fluids
248 also converges relatively quickly. Therefore, in the following simulations, we
249 use a mesh made of 4.3×10^4 elements.

250 4. Results

251 The results of the cocurrent two-phase flows in the aforementioned micro-
252 model are organized as follows. We describe the flow regime observed with

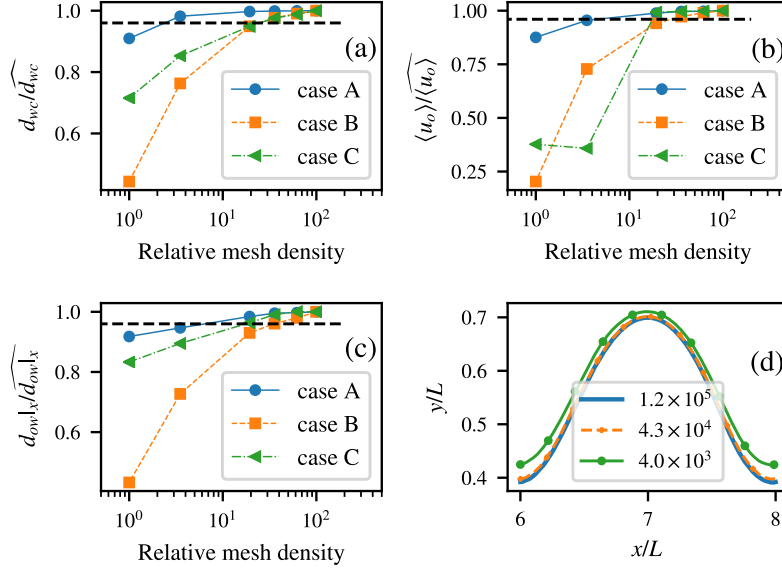


Figure 5: Mesh convergence study of (a) drag force exerted upon the obstacle, (b) intrinsic average velocity of fluid o (c) drag force exerted upon the fluid-fluid boundary and (d) position of the fluid-fluid interface for case B and for different number of mesh elements. All the results are normalized with respect to the result obtained with the finer mesh, denoted with \widehat{symbol} , at steady-state and in UC4. Case A refers to $Ca = 1.25 \times 10^{-1}$, $h^* = 1/4$, case B refers to $Ca = 2.5 \times 10^{-2}$, $h^* = 1/20$ and case C refers to $Ca = 5 \times 10^{-1}$, $h^* = 5$. Other flow parameters are constant, $f_f = 0.25$ and $M = 1$. In the following we use a mesh made of 4.3×10^4 elements.

253 the selected parameters. The regime is fundamental as it drives the extent
 254 of the interfacial surface area between the fluids and therefore the amount of
 255 fluid-fluid drag. The saturation and the fluid-fluid interface are presented as
 256 a function of the gap thickness and capillary numbers. Then we discuss the
 257 effect of the flow confinement, i.e. the permeability, on the velocity and pres-
 258 sure fields. The main section discusses the value of each drag terms presented

259 in Eq. 10.

260 4.1. Flow regimes and fluid saturations

261 As previously discussed, the continuity of the non-wetting phase, and
262 thus the flow regime, may vary in such systems. Here, the continuity of
263 the non-wetting fluid, depends, among other things, on the fractional flow
264 f_f and the ratio of the transverse injection lengths of each fluid y_i/L . We
265 observed breakup of the non-wetting fluid for high fractional flow and small
266 section of injection of this fluid, as shown in Fig. 6. The state diagram was
267 obtained for $Ca = 2.5 \times 10^{-2}$ and a thin gap $h^* = 1/20$, which is the most
268 favorable case for phase breakage, due to greater capillary effects, among the
269 parameters we used. We focus on the film-flow regime in the following, so we
270 chose to perform all the simulations with a low fractional flow ($f_f = 0.25$)
271 and a medium inlet section ($y_o/L = 0.5$). For these parameters, we observed
272 that the two fluids remain continuous at all times and for the entire range
273 of tested capillary numbers and gap thickness, as described in Table 3. The
274 interface between the fluids becomes stationary and steady-state is reached
275 for every capillary number and values of gap thickness.

276 As an example, Fig. 7 shows the initial, intermediate, and final config-
277 urations of the fluid distribution for $Ca = 1.25 \times 10^{-1}$ and $h^* = 1/8$. The
278 fluid-fluid interface is periodic on the five central unit cells at steady-state
279 whereas the interface is slightly deformed at the inlet and outlet cells, under
280 the influence of boundary conditions.

281 The penetration of the non-wetting fluid shown in Fig. 7 does not result
282 from an unstable displacement, i.e. viscous fingering, since both fluids have
283 the same viscosity. Here, non-wetting phase break-up could have occurred

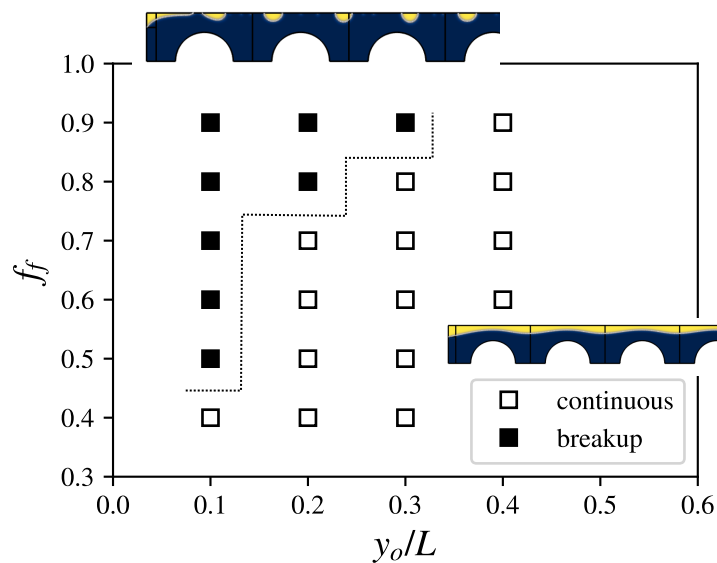


Figure 6: State diagram of the non-wetting phase (in yellow) connectivity during cocurrent two-phase flows in our modified Hele-Shaw cell. The results are given as a function of the fractional flow and the dimensionless inlet length of the non-wetting fluid y_o/L . Here, $h^* = 1/20$ and $Ca = 2.5 \times 10^{-2}$. Breakup of the non-wetting fluid occurred for high fractional flow and small dimension of the inlet.

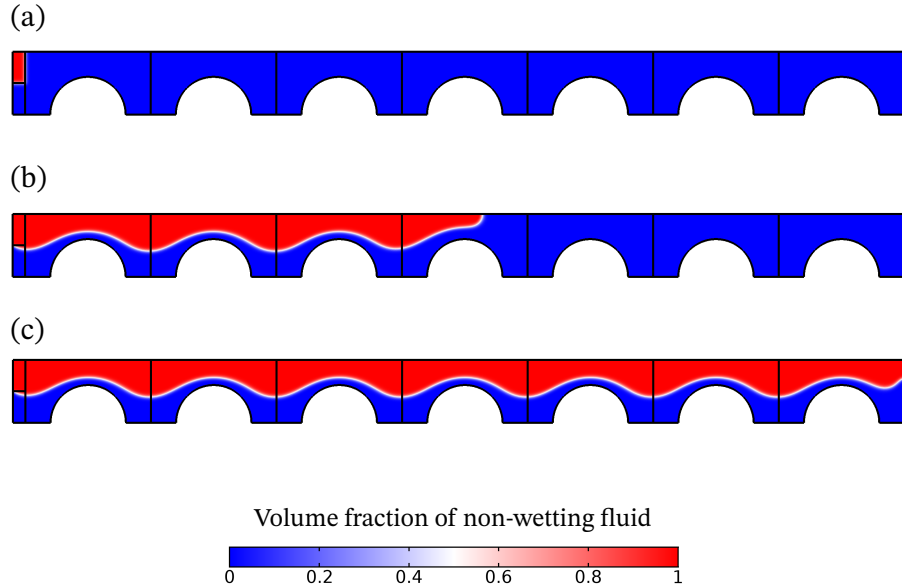


Figure 7: Fluids distribution along the upper half-row at (a) the initial time, (b) an intermediate time and (c) the final time (steady-state reached) for $Ca = 1.25 \times 10^{-1}$, $f_f = 0.25$, $M = 1$ and $h^* = 1/8$. At steady-state the fluid-fluid interface taken on the central unit cells is periodic whereas it is slightly deformed in the first and last UC under the influence of the boundary conditions.

284 either by snap-off phenomenon or because of the shear exerted by the wet-
 285 ting fluid. However, the pore throat is large and the fractional flow is low,
 286 which favors the continuity of the non-wetting fluid phase. The flow-regime
 287 observed is therefore a film-flow regime within the limit of the parameters
 288 chosen for this study.

289 Fig. 8 shows the wetting fluid saturation at steady-state as a function of
 290 the dimensionless gap between the plates and for different capillary numbers.
 291 Wetting fluid saturation at steady-state decreases, on average, from 0.6 to
 292 0.4 as the dimensionless gap between the plates decreases from 5 to $1/20$.

293 The results for the largest gaps are very close to the purely 2D results. The
294 saturation fields insets in Fig. 8 indicate that the fluid-fluid interfaces are
295 very similar for the thinnest gaps, whereas they differ significantly according
296 to the capillary number for thicker gaps. This last point explains the differ-
297 ent saturation we observed. Indeed, for low capillary numbers, the interface
298 is flatter than for high capillary numbers, as shown in Fig. 9. Two config-
299 urations are possible, either the capillary number is high and the fluid-fluid
300 interface is mostly translated toward the pore throat as the gap increases, or
301 the capillary number is low enough that the fluid-fluid interface is deformed
302 (flattened) and also pushed towards the pore throat for an increasing gap
303 thickness. Another important feature that plays a role at the interfacial drag
304 is the symmetry of the fluid-fluid interface, as can be seen from Fig. 9. The
305 interface tends to be symmetric when the gap becomes very thin for any
306 capillary number, and it also tends to be symmetric, whatever the gap, when
307 the capillary number is large. These different fluid configurations might lead
308 to substantial differences in the velocity and pressure fields, for example by
309 forming a narrow channel with high local velocity, which would also impact
310 the amount of drag.

311 *4.2. Pressure and velocity fields*

312 Fig. 10 shows the pressure field for selected values of capillary number
313 and gap thickness. The main result here is that the pressure jump across
314 the fluid-fluid interface is very difficult to distinguish for the largest value of
315 the capillary number $Ca = 5 \times 10^{-1}$, especially for the thinnest gap. This is
316 because the main pressure contribution to the pressure jump arises from the
317 out-of-plane curvature and thus scales as h^{-1} , whereas the pressure gradient

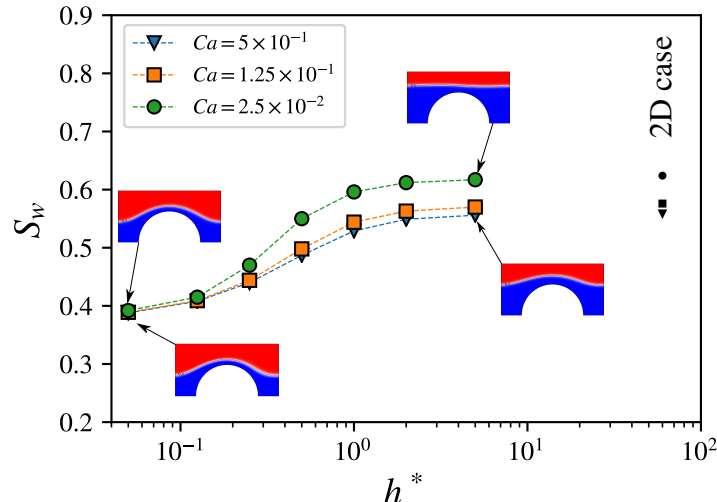


Figure 8: Fluid saturation at steady-state in UC4 as a function of the dimensionless gap and for different capillary numbers. Fields of the level-set function at steady-state in UC4 are given for the selected value of the dimensionless gap and $Ca = 1.25 \times 10^{-1}$. Wetting fluid hold-up increases for thicker gaps. The 2D limit case is given with plain black markers.

318 across the cell scales as h^{-2} for the very thin gap, for which the Darcean
 319 terms are expected to be dominant. In contrast, the pressure jump is visible
 320 for the smallest value of the capillary number $Ca = 2.5 \times 10^{-2}$. In this last
 321 case, we see that the pressure is higher in the non-wetting fluid, which is in
 322 agreement with the orientation of the out-of-plane meniscus.

323 Fig. 11 shows the velocity field, normalized with respect to the reference
 324 velocity, for the same parameters as for the pressure fields. The corresponding
 325 streamlines and the position of the fluid-fluid interface are also presented for
 326 three different cases. For the thinnest gap ($h^* = 1/20$), the velocity fields are
 327 alike regardless of the capillary number. In this case, the maximum velocity is

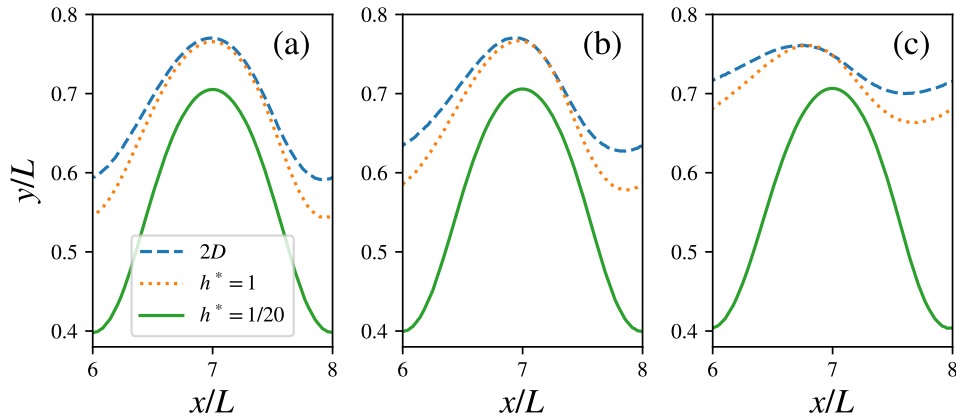


Figure 9: Comparison of the fluid-fluid interface at steady-state in UC4 for different dimensionless gaps between the plates. The interfaces are almost symmetric about the y -axis for a very thin gap for (a) $Ca = 5 \times 10^{-1}$ and (b) $Ca = 1.25 \times 10^{-1}$. The interfaces are flattened for larger gaps for (c) $Ca = 2.5 \times 10^{-2}$. Here, $f_f = 0.25$ and $M = 1$).

328 reached in the center of the pore throat and between the fluid-fluid interface
 329 and the obstacle boundary. For the thickest gap, the velocity field depends on
 330 the capillary number. Either the capillary number is high and the maximum
 331 velocity is reached precisely in the center of the pore throat or the capillary
 332 number is low and the maximum velocity is slightly offset from the center
 333 overhang the fluid interface directly where it forms a narrower constriction.
 334 In this case, we also notice that recirculation cells develop in the wetting
 335 fluid. This observation is a direct manifestation of the momentum transfer
 336 between the two fluids (see also Alamooti et al. (2020)) and indicates that the
 337 fluid-fluid interface should not be treated similarly to fluid/solid boundaries,
 338 or at least not as a fixed wall. In the following, we study the drag force terms
 339 between phases and the effect of permeability and capillary number on them.

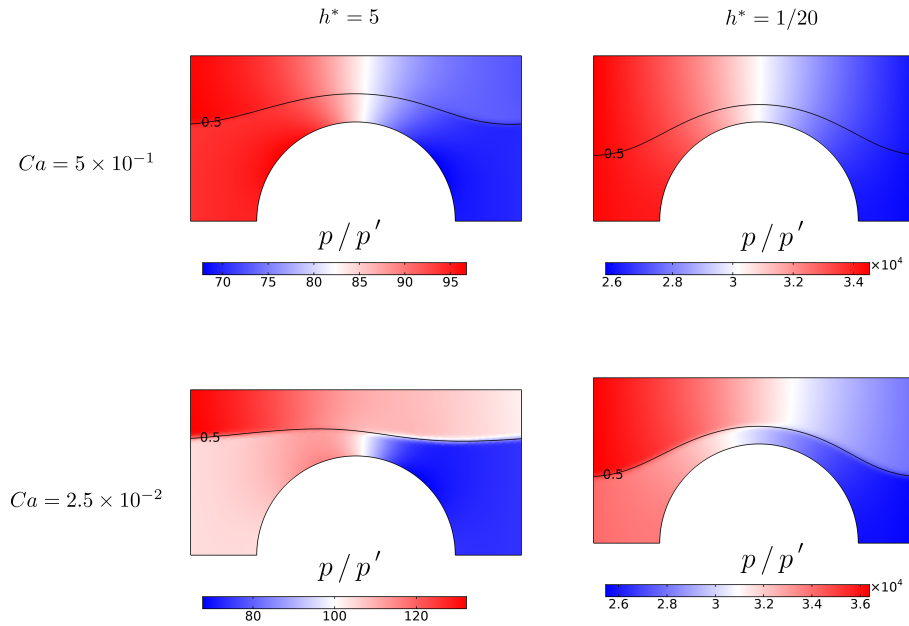


Figure 10: Comparison of the pressure field for two capillary numbers $Ca = 5 \times 10^{-1}$ (top row), $Ca = 2.5 \times 10^{-2}$ (bottom row) and two dimensionless gap thickness, with $h^* = 5$ (left column) and $h^* = 1/20$ (right column). The solid black line denotes the fluid-fluid interface given by the contour $\phi = 0.5$. Results in UC4 at steady-state for $f_f = 0.25$ and $M = 1$. The pressure jump across the fluid is not discernable for a high capillary number, regardless of the gap's thickness, as opposed to pressure fields for a small capillary number.

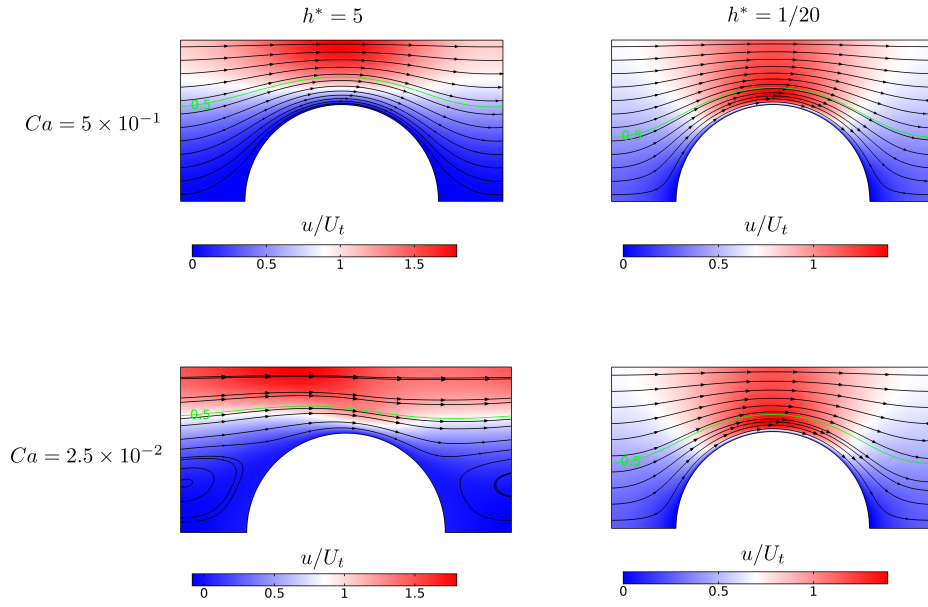


Figure 11: Comparison of the velocity field for two capillary numbers $Ca = 5 \times 10^{-1}$ (top row), $Ca = 2.5 \times 10^{-2}$ (bottom row) and two dimensionless gap thickness, with $h^* = 5$ (left column) and $h^* = 1/20$ (right column). The solid green line denotes the fluid-fluid interface given by the contour $\phi = 0.5$. Results in UC4 at steady-state for $f_f = 0.25$ and $M = 1$. Recirculation cells appeared for low capillary number and thin gaps, which illustrate the momentum transfer from the core fluid o to the wetting fluid w .

340 *4.3. Drag forces between phases*

341 We are only interested in the x -component of the drag forces, d_{ij} , because
 342 it is the main flow direction and we expect that $\partial_y p_i \ll \partial_x p_i$. We also know
 343 from the symmetry of the problem that the gradient of the average pressure
 344 in the y -direction is zero. We start from the sum of the superficial mean
 345 pressure drops, from Eqs. 10,

$$\underbrace{\partial_x \langle p_w \rangle + \partial_x \langle p_o \rangle}_{\partial_x P} = - \underbrace{\frac{12}{h^2} (\mu_w \langle u_w \rangle + \mu_o \langle u_o \rangle)}_{d_s} + d_{wc} + d_{ow} + d_{wo}, \quad (17)$$

346 with $\partial_x P$ the total pressure drop and d_s the sum of all fluid-solid drag forces.
 347 The two pressure drops are plotted against the dimensionless gap thickness
 348 for different capillary numbers in Fig. 12. Both mostly depend on the gap
 349 thickness. For large gaps $h^* \geq 1/2$, the pressure drops tend gently towards
 350 the smaller pressure drop obtained for 2D flow. For smaller gaps $h^* < 1/2$,
 351 the pressure drops scale as h^{-2} , the same as the drag upon the plates. We
 352 noticed that, if $d_{wo} \approx -d_{ow}$, then $\partial_x P \approx d_s$, recalling that d_{ij} stands for the
 353 x -component of the drag force \mathbf{d}_{ij} . To check whether this is the case, we
 354 calculated the following integral, from Eq. 6,

$$d_{wo} = -d_{ow} + \underbrace{\int_{\Gamma_{ow}} \gamma \left(\frac{\pi}{4} \kappa_{\parallel} + \frac{2}{h} \cos \theta \right) \mathbf{n}_{ow} \cdot \mathbf{e}_x \, d\Gamma}_{I_c}. \quad (18)$$

355 Fig. 13 shows the integral I_c normalized with respect to the fluid-fluid drag.
 356 Ratio between I_c and d_{ow} is at a maximum (≈ 0.1) for the smaller Ca and
 357 $h^* = 1/4$, then it decreases for thinner gaps, since the fluid-fluid interface
 358 tends to be symmetric about the y -axis, thus $\int_{\Gamma_{ow}} \mathbf{n}_{ow} \cdot \mathbf{e}_x \, d\Gamma$ tends to zero. In

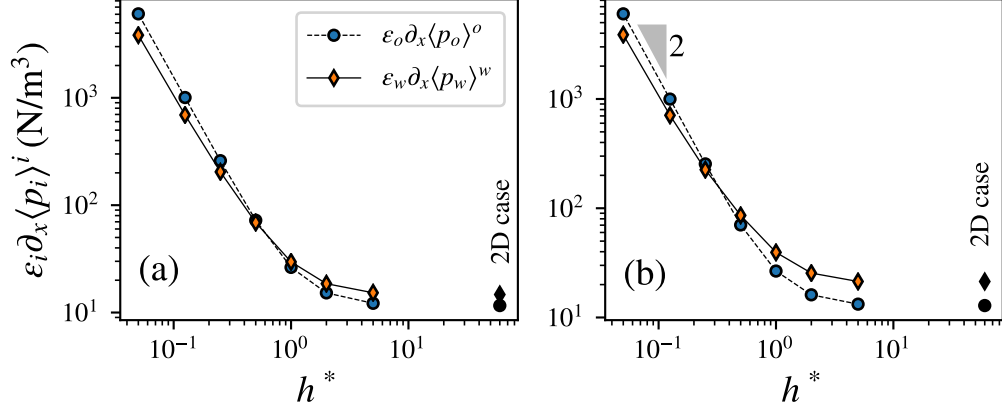


Figure 12: Pressure drop across the model as a function of the dimensionless gap thickness for each fluid. (a) $Ca = 5 \times 10^{-1}$ and (b) $Ca = 2.5 \times 10^{-2}$. Here, $M = 1$, $f_f = 0.25$ and the results are in UC4. The results from 2D Stokes equation are given with the black markers. The pressure drop scales as h^{-2} for thin gaps $h^* \leq 1/4$ for all values of Ca .

359 I_c , the contribution from the out-of-plane meniscus dominates by an order of
 360 magnitude over the contribution of the in-plane curvature for small gaps $h^* \leq$
 361 $1/4$, whereas both contributions are equivalent for larger gaps. Consequently,
 362 the fluid-fluid drag contributions cancel each other in Eq. 17, $d_{wo} \approx -d_{ow}$ in
 363 the following and the total pressure drop is approximately equal to the sum
 364 of the fluid-solid drag.

365 Fig. 14 shows the relative part of each fluid-solid drag force in the total
 366 pressure drop ($\partial_x P$). For 2D flows, the total pressure drop is entirely due to
 367 the wetting fluid drag upon the cylinder. For very thin gaps, about half of
 368 the mean pressure drop is due to the drag upon the cylinder, whereas the
 369 other half is due to the drag upon the plates. In all cases, the total pressure
 370 drop can be approximated by the sum of all the fluid-solid drag forces, as

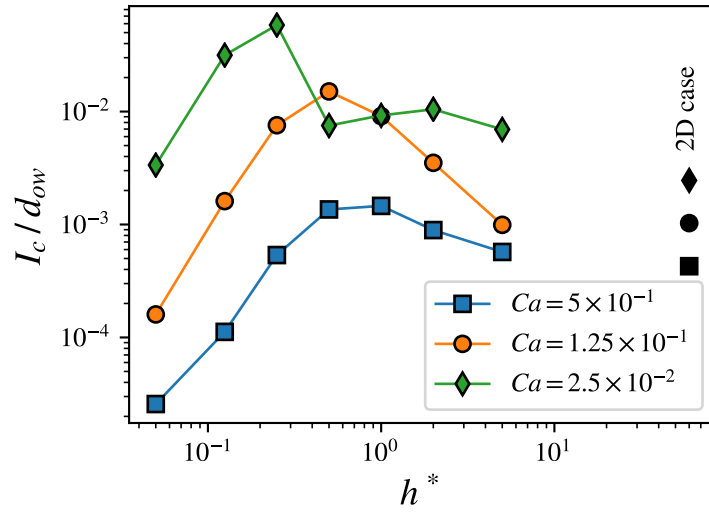


Figure 13: Value of the integral I_c in Eq. 18, non-dimensionalized by the fluid-fluid drag, as a function of the dimensionless gap thickness. Here, $M = 1$, $f_f = 0.25$ and the results are in UC4. The results from 2D Stokes equation are given with the black markers.

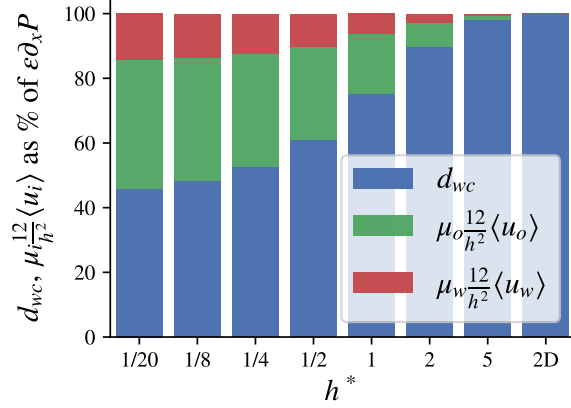


Figure 14: Part of the total mean pressure drop produced by the drag upon the obstacle and upon the plates by each fluid for different dimensionless gap thickness. Results are given for $Ca = 5 \times 10^{-1}$ only since the allocation is very alike for other value of Ca . Here, $M = 1$, $f_f = 0.25$ and the results are in UC4 at steady-state. The total pressure drop is the sum of the mean pressure gradient of each fluid ($\nabla P = \nabla \langle p_w \rangle + \nabla \langle p_o \rangle$).

371 predicted by Eq. 17.

372 We now turn to the fluid-fluid drag force. Fig. 15 shows the part of each
373 drag force in the pressure drop of the non-wetting fluid and wetting fluid.
374 Focusing on the fluid-fluid drag, we notice that its part in the pressure drop
375 is not negligible, even for very thin gaps, since it reaches approximately 40%
376 of $\partial_x \langle p_i \rangle$ for $h^* = 1/20$, whatever the value of Ca . This part increases for
377 thicker gaps (i.e. for higher permeability) up to the maximum value reached
378 for the 2D flow. As an example, the pressure drop of the non-wetting fluid is,
379 logically, entirely due to the fluid-fluid drag force for a 2D flow. Now, looking
380 at the other drags, we notice that the drag upon the obstacle is higher than
381 the drag upon the plates, the former generates, at least, approximately 60%
382 of the pressure drop of the wetting fluid. It is interesting to observe that

383 the relative part of each drag remains quite constant for thin gaps $h^* < 1/4$,
 384 which indicates that for thin gaps all the drag forces scales the same, and
 385 precisely scale as h^{-2} , as previously observed by looking at the pressure
 386 drops. A discrepancy is observable between the pressure drop and the sum
 387 of the drags for thick gaps and small Ca , due to the approximations when
 388 considering that the two drag forces are equal. Finally, the main findings here
 389 are that the fluid-fluid drag force is non-negligible compared to the fluid-solid
 390 drag forces and that the relative importance of this drag increases with the
 391 gap, therefore with the permeability. We also observe that the relative part of
 392 each drag is constant for very thin gaps $h^* \leq 1/4$. In the following paragraph,
 393 we present a scaling argument to explain this finding.

394 The limit case of very thin gaps is best described by Darcy's law. The
 395 pressure drag can be written as $d_{ij}^p = -\frac{1}{S} \int p_i \mathbf{n}_{ij} \cdot \mathbf{e}_x d\Gamma$ and the viscous drag
 396 as $d_{ij}^\mu = \left(\frac{1}{S} \int \mu_i \nabla \langle u_i \rangle \cdot \mathbf{n}_{ij} d\Gamma \right) \cdot \mathbf{e}_x$. Estimation of the pressure is given, in
 397 the thin-gap regime, by Darcy's law as $p \approx L \langle u \rangle \mu / h^2$. Since the viscous
 398 stress can be estimated as $\mu \langle u \rangle / L$, the ratio between these two terms scales
 399 as L/h , and the viscous drag is negligible in front of the pressure drag when
 400 $L/h \gg 1$. Now, the pressure term is applied on a contour of length L , so
 401 $d_f^p \approx \langle u \rangle \mu / h^2$. Consequently, the pressure drag at the fluid-fluid interface
 402 scales as the drag upon the plates. The features of the thin-gap regime,
 403 defined as $h^* \leq 1/4$, are (i) the pressure drag dominates over the viscous
 404 drag, which is negligible, and (ii) the pressure drag scales as the drag upon
 405 the plates, and the fluid-fluid drag is not negligible. All drag forces scale the
 406 same in this latter regime.

407 This scaling reasoning can be checked by looking at the pressure and

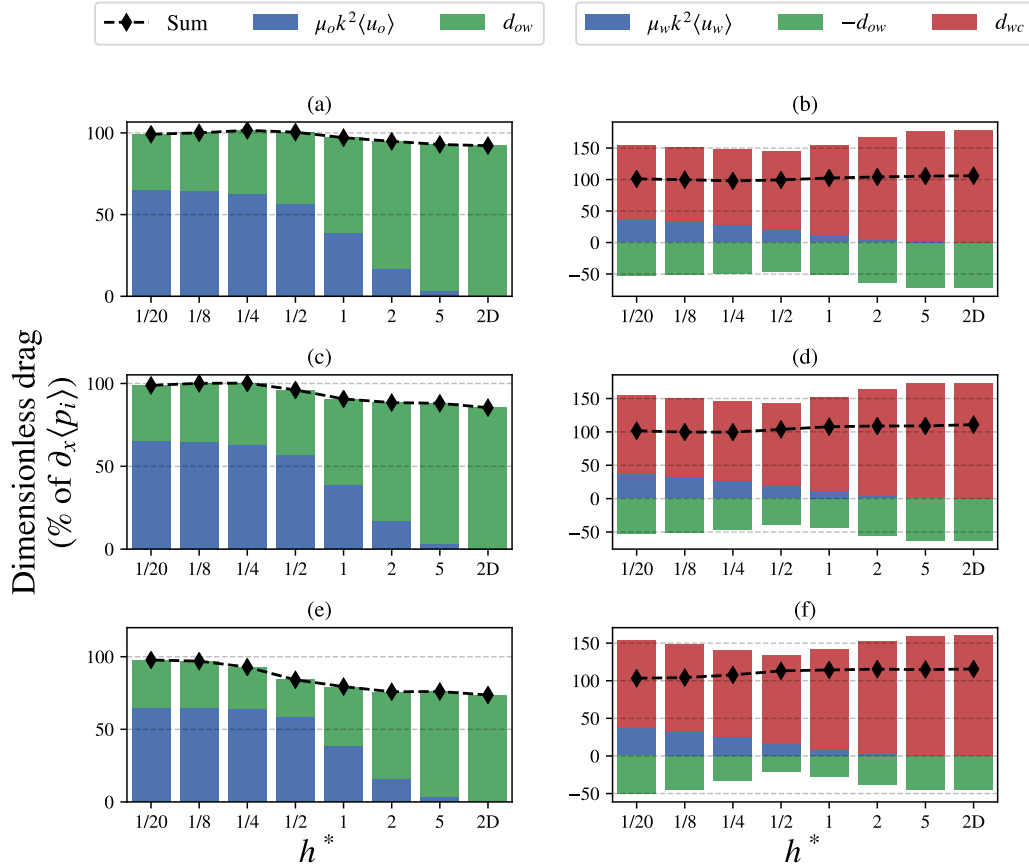


Figure 15: Part of the drag forces in the mean pressure gradient of a given fluid. Results are given for each dimensionless gap thickness and capillary number. (a) fluid *o* and (b) fluid *w* for $Ca = 5 \times 10^{-1}$, (c) fluid *o* and (d) fluid *w* for $Ca = 1.25 \times 10^{-1}$, (e) and (f) fluid *o* and *w*, respectively, for $Ca = 2.5 \times 10^{-2}$. The sum of all drag forces is given with the black markers. Here, $M = 1$, $f_f = 0.25$, and the results are in UC4 after steady-state was reached. The discrepancy for thick gaps and low Ca comes from the approximation made by considering that the fluid-fluid drag forces are equal.

408 viscous drag in the fluid-fluid drag force

$$d_{ij} = \underbrace{\frac{1}{S} \int_{\Gamma_{ij}} -p_i \mathbf{n}_{ij} \cdot \mathbf{e}_x \, d\Gamma}_{d_{ij}^p} + \underbrace{\frac{1}{S} \int_{\Gamma_{ij}} \mathbf{n}_{ij} \cdot \mu_i \left(\nabla \mathbf{u}_i + (\nabla \mathbf{u}_i)^T \right) \cdot \mathbf{e}_x \, d\Gamma}_{d_{ij}^\mu}. \quad (19)$$

409 Fig. 16 shows the relative part of the viscous (d_f^μ) and pressure terms
 410 (d_f^p) in the fluid-fluid drag. The viscous term is negligible compared to the
 411 pressure part for very thin gaps $h^* \leq 1/4$ and for every value of Ca , as
 412 previously shown. In contrast, the viscous drag dominates over the pressure
 413 drag for low Ca and very thick gaps. Both terms are important for high Ca
 414 and thick gaps/2D flow.

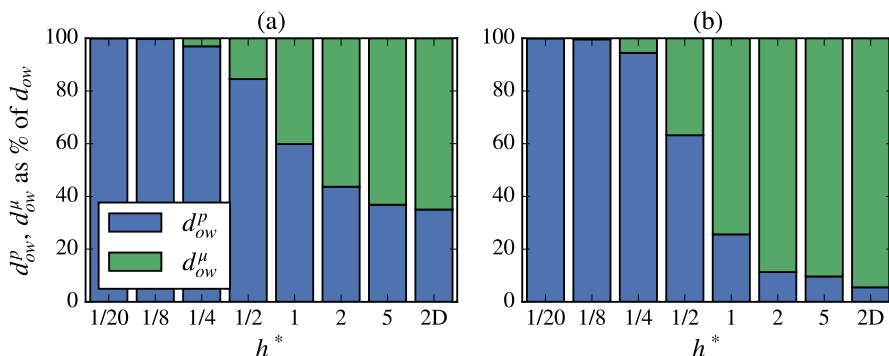


Figure 16: Part of viscous and pressure drag into the fluid-fluid drag force for different dimensionless gap thickness. (a) $Ca = 5 \times 10^{-1}$ and (b) $Ca = 2.5 \times 10^{-2}$. Here, $M = 1$, $f_f = 0.25$, and the results are obtained in UC4 at steady-state. The viscous drag is negligible compared to the pressure drag for thin gap $h^* \leq 0.25$.

415 5. Conclusions

416 The question of active or passive fluid-fluid interface (i.e. allows or not
 417 momentum exchange from one fluid to another) is of major concern for two-

418 phase flows in microfluidic devices, and by extension in porous media. This
419 issue has been treated recently for remobilization of ganglia, for which the
420 drag exerted by the surrounding flowing fluid is capital. Although not man-
421 ifesting itself in such a visual way, fluid-fluid drag may also be important in
422 the case of continuous film flow (i.e. the two fluids are flowing adjacently
423 in the same channel), as the common interface is large. We addressed this
424 question by numerical simulations in a modified Hele-Shaw cell, which al-
425 lows calculating the contribution from the viscous shear, but also from the
426 pressure contrary to the previous work, in the fluid-fluid drag.

427 We found that the fluid-fluid drag is not negligible, even for small gaps
428 between the cell's plate (i.e. increasing solid-fluid friction). For an increasing
429 gap, the fluid-fluid drag is more and more important to predict the pressure
430 drop, especially for high capillary numbers. As an example, for $Ca = 0.5$,
431 the fluid-fluid drag represents between 30% to 65% of the non-wetting fluid's
432 pressure drop for a dimensionless gap increasing from $1/20$ to 1. Also, we
433 found that the pressure contribution may overcome the viscous shear contri-
434 bution for smaller gaps.

435 The main limit of this work is the presence of the cylindrical solid ob-
436 stacles between the cell's plates, also discussed in past similar works. The
437 no-flow boundary condition induced a more complex flow field near the ob-
438 stacle that is not well reproduced by the depth-averaged 2D flow equation.
439 However, this issue is not strengthened by increasing the gap, which allows
440 us to compare the results as we have done. These findings are important
441 to predict and model two-phase flows in microfluidic devices when film-flow
442 regimes are expected. They also add arguments in favor of taking into ac-

443 count the coupling between the two fluids in the large-scale flow equations
444 used for highly permeable media, as film flow is a common regime in such
445 porous media. Further work could investigate the dynamic film effects in the
446 case of zero contact angle between the cell plates and the impact on the drag
447 forces on them. However, this likely requires computationally intensive 3D
448 flow calculations in order to accurately capture the films.

449 **6. Acknowledgements**

450 This work was supported by the French Geological Survey (BRGM) within
451 the framework of the PSO MULTISCALEXPER project. The authors would
452 like to thank the French Environment and Energy Management Agency
453 (ADEME) and BRGM for providing the Ph.D. grant for Maxime Cochenec.
454 We gratefully acknowledge the financial support provided to the PIVOTS
455 project by the “Région Centre – Val de Loire” and the European Regional
456 Development Fund.

457 **References**

- 458 Alamooti, A.H.M., Azizi, Q., Davarzani, H., 2020. Direct numerical simula-
459 tion of trapped-phase recirculation at low capillary number. *Advances in*
460 *Water Resources* 145, 103717.
- 461 Anderson, W.G., et al., 1987. Wettability literature survey part 5: the effects
462 of wettability on relative permeability. *Journal of Petroleum Technology*
463 39, 1–453.
- 464 Attou, A., Boyer, C., Ferschneider, G., 1999. Modelling of the
465 hydrodynamics of the cocurrent gas–liquid trickle flow through a

466 trickle-bed reactor. *Chemical Engineering Science* 54, 785 – 802.
467 doi:[https://doi.org/10.1016/S0009-2509\(98\)00285-1](https://doi.org/10.1016/S0009-2509(98)00285-1).

468 Auriault, J., Sanchez-Palencia, E., 1986. Remarques sur la loi de darcy pour
469 les écoulements biphasiques en milieu poreux. *Journal of Theoretical and*
470 *Applied Mechanics*, Numéro Spécial , p141–156.

471 Avraam, D.G., Payatakes, A.C., 1995. Generalized relative permeability co-
472 efficients during steady-state two-phase flow in porous media, and corre-
473 lation with the flow mechanisms. *Transport in Porous Media* 20, 135–168.
474 doi:10.1007/bf00616928.

475 Ayodele, O.R., 2006. Theoretical analysis of viscous coupling in two-phase
476 flow through porous media. *Transport in porous media* 64, 171–184.

477 Ayub, M., Bentsen, R.G., 1999. Interfacial viscous coupling: a myth or
478 reality? *Journal of Petroleum Science and Engineering* 23, 13–26.

479 Bacri, J.C., Chaouche, M., Salin, D., 1990. Modèle simple de perméabilités
480 relatives croisées. *Comptes rendus de l'Académie des sciences. Série 2,*
481 *Mécanique, Physique, Chimie, Sciences de l'univers, Sciences de la Terre*
482 311, 591–597.

483 Bashir, S., Rees, J.M., Zimmerman, W.B., 2014. Investigation of pressure
484 profile evolution during confined microdroplet formation using a two-phase
485 level set method. *International journal of multiphase flow* 60, 40–49.

486 Bensimon, D., 1986. Stability of viscous fingering. *Physical Review A* 33,
487 1302.

- 488 Bentsen, R.G., Manai, A.A., 1993. On the use of conventional cocurrent
489 and countercurrent effective permeabilities to estimate the four generalized
490 permeability coefficients which arise in coupled, two-phase flow. *Transport*
491 *in Porous Media* 11, 243–262.
- 492 Bianchi Janetti, E., Riva, M., Guadagnini, A., 2017. Effects of pore-scale
493 geometry and wettability on two-phase relative permeabilities within ele-
494 mentary cells. *Water* 9, 252.
- 495 Blunt, M.J., 2017. *Multiphase flow in permeable media: A pore-scale per-*
496 *spective*. Cambridge University Press.
- 497 Bourbiaux, B.J., Kalaydjian, F.J., et al., 1990. Experimental study of cocur-
498 rent and countercurrent flows in natural porous media. *SPE Reservoir*
499 *Engineering* 5, 361–368.
- 500 Brooks, R., Corey, T., 1964. Hydraulic properties of porous media. *Hydrolog-*
501 *ogy Papers, Colorado State University* 24, 37.
- 502 Chen, J., Sun, S., Wang, X., 2019. Homogenization of two-phase fluid flow
503 in porous media via volume averaging. *Journal of Computational and*
504 *Applied Mathematics* 353, 265–282.
- 505 Clavier, R., Chikhi, N., Fichot, F., Quintard, M., 2017. Modeling of iner-
506 tial multi-phase flows through high permeability porous media: Friction
507 closure laws. *International Journal of Multiphase Flow* 91, 243–261.
- 508 Cueto-Felgueroso, L., Juanes, R., 2014. A phase-field model of two-phase
509 hele-shaw flow. *Journal of fluid mechanics* 758, 522.

510 Davit, Y., Quintard, M., 2018. One-phase and two-phase flow in highly
511 permeable porous media. *Heat Transfer Engineering* , 1–19.

512 Dullien, F.A., 1992. *Porous media: fluid transport and pore structure*. 2 ed.,
513 Academic press.

514 Dullien, F.A.L., Dong, M., 1996. Experimental determination of the flow
515 transport coefficients in the coupled equations of two-phase flow in porous
516 media. *Transport in Porous Media* 25, 97–120. doi:10.1007/bf00141264.

517 Ehrlich, R., 1993. Viscous coupling in two-phase flow in porous media and its
518 effect on relative permeabilities. *Transport in Porous Media* 11, 201–218.

519 Fetter, C.W., Boving, T., Kremer, D., 2017. *Contaminant hydrogeology*.
520 Waveland Press.

521 Gray, W.G., Miller, C.T., 2005. Thermodynamically constrained averaging
522 theory approach for modeling flow and transport phenomena in porous
523 medium systems: 1. motivation and overview. *Advances in Water Re-*
524 *sources* 28, 161–180.

525 Gray, W.G., Miller, C.T., 2014. *Introduction to the thermodynamically*
526 *constrained averaging theory for porous medium systems*. Springer.

527 Guyon, E., Hulin, J.P., Petit, L., 1994. *Hydrodynamique physique. interédi-*
528 *tions*.

529 Heshmati, M., Piri, M., 2018. Interfacial boundary conditions and residual
530 trapping: A pore-scale investigation of the effects of wetting phase flow

531 rate and viscosity using micro-particle image velocimetry. *Fuel* 224, 560 –
532 578. doi:<https://doi.org/10.1016/j.fuel.2018.03.010>.

533 Homsy, G.M., 1987. Viscous fingering in porous media. *Annual review of*
534 *fluid mechanics* 19, 271–311.

535 Horgue, P., Augier, F., Duru, P., Prat, M., Quintard, M., 2013. Experimental
536 and numerical study of two-phase flows in arrays of cylinders. *Chemical*
537 *Engineering Science* 102, 335–345.

538 Jackson, S., Power, H., Giddings, D., Stevens, D., 2017. The stability of
539 immiscible viscous fingering in hele-shaw cells with spatially varying per-
540 meability. *Computer Methods in Applied Mechanics and Engineering* 320,
541 606–632.

542 Karadimitriou, N., Hassanizadeh, S., 2012. A review of micromodels and
543 their use in two-phase flow studies. *Vadose Zone Journal* 11.

544 Kopf-Sill, A.R., Homsy, G., 1988. Bubble motion in a hele-shaw cell. *The*
545 *Physics of fluids* 31, 18–26.

546 Lasseux, D., Quintard, M., Whitaker, S., 1996. Determination of perme-
547 ability tensors for two-phase flow in homogeneous porous media: theory.
548 *Transport in Porous Media* 24, 107–137.

549 Lenormand, R., Touboul, E., Zarcone, C., 1988. Numerical models and
550 experiments on immiscible displacements in porous media. *Journal of fluid*
551 *mechanics* 189, 165–187.

- 552 Li, H., Pan, C., Miller, C.T., 2005. Pore-scale investigation of viscous cou-
553 pling effects for two-phase flow in porous media. *Physical Review E* 72.
554 doi:10.1103/physreve.72.026705.
- 555 Liu, J., Ju, Y., Zhang, Y., Gong, W., 2019. preferential paths of air-water
556 two-phase flow in porous structures with special consideration of channel
557 thickness effects. *Scientific reports* 9, 1–13.
- 558 Marle, C.M., 1982. On macroscopic equations governing multiphase flow with
559 diffusion and chemical reactions in porous media. *International Journal*
560 *of Engineering Science* 20, 643 – 662. doi:[https://doi.org/10.1016/0020-](https://doi.org/10.1016/0020-7225(82)90118-5)
561 [7225\(82\)90118-5](https://doi.org/10.1016/0020-7225(82)90118-5).
- 562 Maruvada, S., Park, C.W., 1996. Retarded motion of bubbles in hele–shaw
563 cells. *Physics of fluids* 8, 3229–3233.
- 564 Maxworthy, T., 1986. Bubble formation, motion and interaction in a hele-
565 shaw cell. *Journal of Fluid Mechanics* 173, 95–114.
- 566 Meiburg, E., Homsy, G., 1988. Nonlinear unstable viscous fingers in hele–
567 shaw flows. ii. numerical simulation. *The Physics of fluids* 31, 429–439.
- 568 Morrow, N.R., Cram, P.J., McCaffery, F., et al., 1973. Displacement studies
569 in dolomite with wettability control by octanoic acid. *Society of Petroleum*
570 *Engineers Journal* 13, 221–232.
- 571 Muskat, M., 1938. The flow of homogeneous fluids through porous media.
572 *Soil Science* 46, 169.

573 Nagel, M., Gallaire, F., 2015. Boundary elements method for microfluidic
574 two-phase flows in shallow channels. *Computers & Fluids* 107, 272–284.

575 Olsson, E., Kreiss, G., 2005. A conservative level set method for
576 two phase flow. *Journal of Computational Physics* 210, 225 – 246.
577 doi:<https://doi.org/10.1016/j.jcp.2005.04.007>.

578 Olsson, E., Kreiss, G., Zahedi, S., 2007. A conservative level set method
579 for two phase flow ii. *Journal of Computational Physics* 225, 785 – 807.
580 doi:<https://doi.org/10.1016/j.jcp.2006.12.027>.

581 Park, C.W., Homsy, G., 1984. Two-phase displacement in hele shaw cells:
582 theory. *Journal of Fluid Mechanics* 139, 291–308.

583 Rakotomalala, N., Salin, D., Yortsos, Y.C., 1995. Viscous coupling in a model
584 porous medium geometry: Effect of fluid contact area. *Applied scientific*
585 *research* 55, 155–169.

586 Ramakrishnan, T.S., Goode, P.A., 2015. Measurement of off-diagonal trans-
587 port coefficients in two-phase flow in porous media. *Journal of colloid and*
588 *interface science* 449, 392–398.

589 Roman, S., Soullaine, C., Kovscek., A.R., 2019. Pore-scale visualization and
590 characterization of viscous dissipation in porous media. *Journal of Colloid*
591 *and Interface Science* doi:<https://doi.org/10.1016/j.jcis.2019.09.072>.

592 Rose, W., 1988. Measuring transport coefficients necessary for
593 the description of coupled two-phase flow of immiscible fluids in
594 porous media. *Transport in Porous Media* 3, 163–171. URL:
595 <https://doi.org/10.1007/BF00820343>, doi:10.1007/BF00820343.

- 596 Rothman, D.H., 1990. Macroscopic laws for immiscible two-phase flow in
597 porous media: Results from numerical experiments. *Journal of Geophysical*
598 *Research* 95, 8663. doi:10.1029/jb095ib06p08663.
- 599 Saffman, P.G., Taylor, G.I., 1958. The penetration of a fluid into a porous
600 medium or hele-shaw cell containing a more viscous liquid. *Proceedings of*
601 *the Royal Society of London. Series A. Mathematical and Physical Sciences*
602 245, 312–329.
- 603 de Santos, J.M., Melli, T.R., Scriven, L.E., 1991. Mechanics of gas-liquid flow
604 in packed-bed contactors. *Annual Review of Fluid Mechanics* 23, 233–260.
605 doi:10.1146/annurev.fl.23.010191.001313.
- 606 Schmidt, W., 2007. Interfacial drag of two-phase flow in porous me-
607 dia. *International Journal of Multiphase Flow* 33, 638 – 657. URL:
608 <http://www.sciencedirect.com/science/article/pii/S0301932206001662>,
609 doi:<https://doi.org/10.1016/j.ijmultiphaseflow.2006.09.006>.
- 610 Scott, P., Rose, W., et al., 1953. An explanation of the yuster effect. *Journal*
611 *of Petroleum Technology* 5, 19–20.
- 612 Stokes, J., Weitz, D., Gollub, J.P., Dougherty, A., Robbins, M., Chaikin,
613 P., Lindsay, H., 1986. Interfacial stability of immiscible displacement in a
614 porous medium. *Physical review letters* 57, 1718.
- 615 Van Genuchten, M.T., 1980. A closed-form equation for predicting the hy-
616 draulic conductivity of unsaturated soils 1. *Soil science society of America*
617 *journal* 44, 892–898.

- 618 Whitaker, S., 1986. Flow in porous media II: The governing equations for
619 immiscible, two-phase flow. *Transport in porous media* 1, 105–125.
- 620 Whitaker, S., 1999. *The Method of Volume Averaging*. Springer, Dordrecht.
- 621 Wyckoff, R.D., Botset, H.G., 1936. The flow of gas-liquid mixtures through
622 unconsolidated sands. *Physics* 7, 325–345.
- 623 Yiotis, A.G., Psihogios, J., Kainourgiakis, M.E., Papaioannou, A., Stu-
624 bos, A.K., 2007. A lattice boltzmann study of viscous coupling ef-
625 fects in immiscible two-phase flow in porous media. *Colloids and*
626 *Surfaces A: Physicochemical and Engineering Aspects* 300, 35 – 49.
627 doi:<https://doi.org/10.1016/j.colsurfa.2006.12.045>.
- 628 Yuster, S., et al., 1951. Theoretical considerations of multiphase flow in
629 idealized capillary systems, in: *Proceedings of the Third World Petroleum*
630 *Congress*, E. Brill The Hague. pp. 437–445.
- 631 Zarcone, C., Lenormand, R., 1994. Détermination expérimentale du couplage
632 visqueux dans les écoulements diphasiques en milieu poreux. *Comptes*
633 *rendus de l'Académie des sciences. Série II, Mécanique, physique, chimie,*
634 *astronomie* 318, 1429–1435.
- 635 Zhang, C., Oostrom, M., Wietsma, T.W., Grate, J.W., Warner, M.G., 2011.
636 Influence of viscous and capillary forces on immiscible fluid displacement:
637 Pore-scale experimental study in a water-wet micromodel demonstrating
638 viscous and capillary fingering. *Energy & Fuels* 25, 3493–3505.

639 **Appendix A. Comparison between 3D and depth-averaged 2D one-**
640 **phase flows**

641 In this appendix section we compare 3D and depth-averaged 2D one-
642 phase flows to illustrate the impact of the gap thickness. The geometry is
643 the same as used previously (3D model is obtained by an extrusion). First,
644 Fig. A.17 shows the velocity profile (x -component) along a line from the tip of
645 the cylindrical obstacle to the center of the pore (along y -axis) as a function
646 of the dimensionless gap thickness. We observe a difference between the 2D
647 and 3D results, even for a small gap thickness. This is due to the cylindrical
648 solid obstacles that which locally disturbs the velocity field and which can
649 only be obtained by 3D models. We note that this effect is not amplified
650 by going outside the theoretical validity domain ($h/L \ll 1$), and that the
651 depth-averaged 2D model is still effective.

652 This has an impact on the calculation of the drag on the cylindrical
653 solid obstacle. As shown in Fig. A.18, the drag per unit of surface is well
654 reproduced for gaps as large as $h/L = 2$.

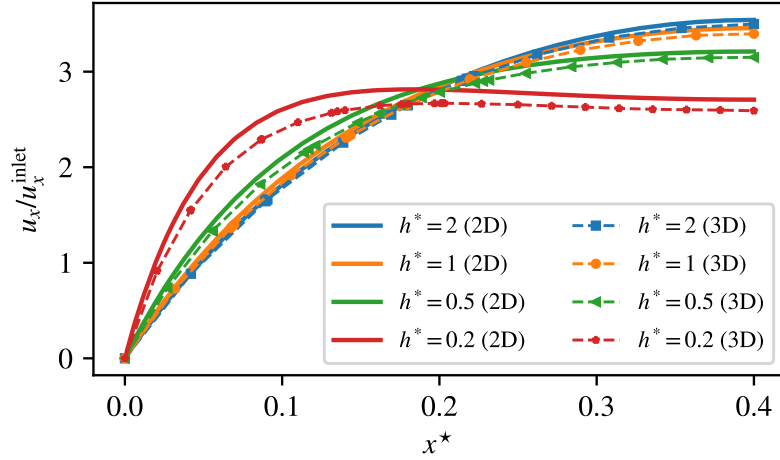


Figure A.17: Normalized velocity (x -component) profile along the line that goes from the tip of the obstacle to the center of the cell (along the y axis), for 2D depth-integrated and integrated 3D flow as a function of the dimensionless gap thickness.

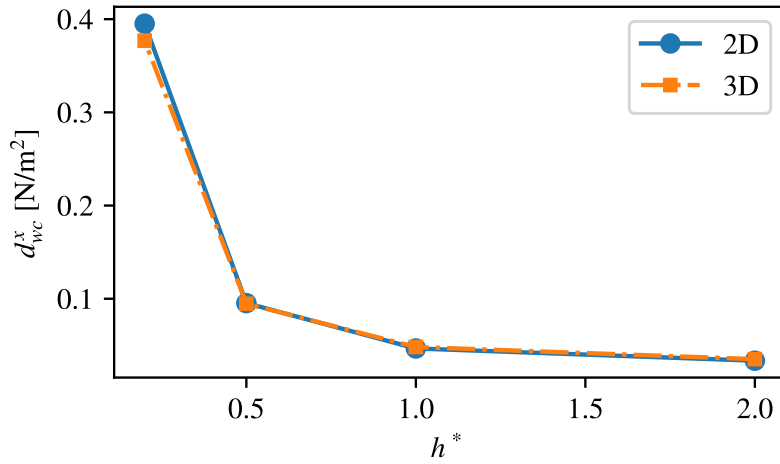


Figure A.18: Drag (x -component) per unit of surface, for 2D depth-integrated and 3D flows as a function of the dimensionless gap thickness.